

Prototype of a Phonon Laser with Trapped Ions

Chen-Yu Lee, Kuan-Ting Lin, and Guin-Dar Lin

Department of Physics and Center for Theoretical Physics,
National Taiwan University, Taipei 10617, Taiwan

Center for Quantum Science and Engineering, National Taiwan University, Taipei 10617, Taiwan

We propose a tunable phonon laser prototype with a large trapped ion array, where some of the ions are effectively pinned by optical tweezers, thus isolating a subset of ions that mimics an acoustic cavity used as a phonon lasing resonator. The cavity loss can then be controlled by the tweezer strength and the “wall thickness”, the number of pinned ions for isolation. We pump the resonator by applying blue-sideband lasers, and investigate the lasing dynamics of the cavity modes such as threshold behavior, population distribution, the second-order coherence, and line-narrowed spectrum. This scheme can be generalized to resonators consisting of multiple cavity modes formed by a few ions, where we demonstrate mode competition and synchronization as lasing modes have developed.

Introduction. – Laser technology has been one of the most important ingredients in contemporary scientific research, industry, and consumer electronics. Many remarkable properties of an optical laser like quantum coherence and capability to travel over a long distance make it a unique tool in applications of modern quantum engineering and communication. Recently, acoustic analog of lasing phenomena has drawn growing interest. This line of research extends our understanding from ordinary quantum optics to other physical degrees of freedom for their mathematical frameworks share essential similarities. Acoustic waves are much slower than the light and hence of shorter wavelength, thus providing an opportunities for precise phase control. Further, the interaction processes between an atom and phonons can be deterministic without additional waveguides, which is very useful for quantum computing [1].

The first phonon laser was realized in a trapped ion system driven by optical forces [2], where a single ion presents self-sustained oscillation beyond a threshold gaining energy from optical sources. Since then, many proposals have been studied and demonstrated in similar platforms [3, 4] and others such as quantum dots [5–7], and optomechanical systems [7–16]. Many intriguing properties of ordinary lasers have also been reported in phonon systems, including oscillation threshold [2, 8, 10, 11, 13, 15–17], Poissonian distribution [15], linewidth narrowing [8–10, 13, 15, 17], injection locking [3, 4], and mode competition [11, 16]. Most of the schemes, however, are based on sophisticated designs of architecture and cannot be easily scaled up to include more modes. The parameters of the lasing resonator are typically fixed upon fabrication, limiting the opportunities of exploring rich phonon physics.

Here, we propose a prototype of a tunable phonon laser based on a large uniform ion crystal and optical tweezers. Such an ion crystal can be constructed in a long Paul trap [18], microtraps or Penning microtrap arrays [19–21]. We apply optical tweezers on one ion or a few in a row so that they form a “wall” for acoustic waves.

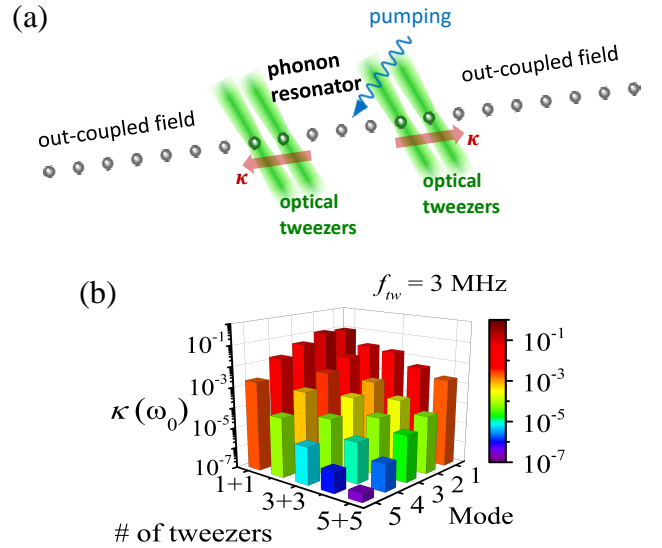


FIG. 1: (a) Architecture of an effective phonon resonator constructed on a large-scale ion crystal. The tweezered ions act as partial mirrors of the resonator. (b) Mode decay rates against varied wall thickness of an $N_S = 5$ cavity. The collective normal modes are ordered according to their frequencies. (1: lowest; 5: highest) These results are based on calculation considering an $N > 2000$ $^{40}\text{Ca}^+$ ion crystal with ion separation $7 \mu\text{m}$.

We then consider a small subset of ions being contained by two such walls, forming an effective phonon cavity as shown in Fig. 1(a). Note that, for a uniform ion crystal, the frequency scale characterizing momentum exchange between adjacent ions is $\omega_0 \equiv [e^2/(4\pi\epsilon_0 m d_0^3)]^{-1/2}$, obtained by matching the energy scales of local oscillation and mutual Coulomb interaction, where e is the charge carried by an ion of mass m . For ion separation d_0 about a few microns, ω_0 is of order of magnitude about hundreds of kilohertz to a few megahertz. Therefore, the application of optical tweezers of strength larger than ω_0 by roughly an order can significantly modify the motional spectrum, resulting in a collection of local modes formed

within the ‘‘cavity’’. This remarkable feature allows us to view the system as a phonon laser resonator.

The beauty of this proposed scheme is its simplicity and flexibility of reconfiguration. Note that optical tweezers can be switched on and off easily at a timescale of nanoseconds, without altering the spatial equilibrium of the array. Further, the effective cavity is scalable in size on demand. The reflectivity of a partial mirror can be tuned by varying tweezer frequencies and/or numbers of tweezers. In following discussion, we demonstrate the idea by looking into the lasing dynamics assuming the ion array is only Doppler cooled.

Model. – We consider N_S ions within the effective resonator, and only focus on N_S longitudinal modes. This is because the rest of the array contribute to a broader dispersion band of bath in the longitudinal modes than the transverse ones. A wall thickness w is represented by the number of tweezered ions. We use $w_L + w_R$ to denote the thicknesses of the left and right walls. Without altering the general conclusion, in this work we look at the symmetric cases with $w_L = w_R$. The number of bath ions is $N_B = N - w_L - w_R - N_S$, where N is the total number of ions. It is assumed that $N_B \gg N_S$ such that the discrete bath spectrum approximate a continuous band and is treated Markovian.

The motional Hamiltonian is described by $H_m = \sum_i p_i^2/(2m) + \sum_{i,j} A_{ij} z_i z_j$, where z labels the longitudinal direction, z_i is coordinate operator with respect to the equilibrium position of the i th ion, and the associated momentum p_i . The coupling matrix elements $A_{ii} = \nu_i^2 + \nu_i^{\text{ot}2} + \sum_{l=1, l \neq i}^N 2/|u_i - u_l|^3$ and $A_{ij} = -2/|u_i - u_j|^3$ for $i \neq j$, where u_i is the equilibrium z position of the i th ion in units of d_0 [22]. Also, $\nu_i = \omega_i/\omega_0$ and $\nu_i^{\text{ot}} = \omega_i^{\text{ot}}/\omega_0$ are dimensionless frequencies introduced by the global trap and optical tweezers, respectively. Here, we use the trap configuration discussed in [18], a large linear Paul trap with a box-like potential so that $\omega_i \approx 0$ except those near the edges, where the exact form of the potential profile needs to be computed with care. We also assume that optical tweezers are applied transversely to the array so $\omega_i^{\text{ot}} > 0$ for tweezered ions; otherwise, $\omega_i^{\text{ot}} = 0$.

By dividing the whole array into the system C [Appendix A] and the bath B , and using the phononic field operator representation, the motional Hamiltonian can be recast into

$$H_m = \sum_{q \in C} \hbar \omega_q a_q^\dagger a_q + \sum_{k \in B} \hbar \omega_k a_k^\dagger a_k + \sum_{q \in C, k \in B} g_{qk} \left(a_q a_k^\dagger + \text{H.c.} \right), \quad (1)$$

where a_q (a_k) and a_q^\dagger (a_k^\dagger) are phononic annihilation and creation operators, respectively, of the q th (k th) normal modes of C (B). H.c. stands for the Hermitian conjugate. The system-bath mode coupling $g_{qk} = g_{kq}^T = \frac{\hbar}{2m} \sum_{i \in C, j \in B} U_{C,qi}^T A_{ij} U_{B,jk} / \sqrt{m^2 \omega_q \omega_k}$, where the ma-

trices U_C and U_B diagonalize the corresponding submatrices in matrix $\mathbf{A} \equiv [A_{ij}]$. Since $N_B \gg N_S$, the excitation within the cavity can dissipate to the bath’s degrees of freedom, and only return after a long time $\sim N_B \omega_0^{-1}$. This timescale is given by the elapsed time of motion propagation to the edge and back. Before the revival happens, the dissipation of the cavity modes can be characterized by the decay rates

$$\kappa_q \approx 2\pi \bar{g}_{qq}^2 \rho_B(\omega_q) \quad (2)$$

according to the standard Fermi golden rule approach. Here, we have taken the continuum limit for B and numerically computed the density of states $\rho_B(\omega)$ of the bath. We obtain \bar{g}_{qq}^2 by coarse-graining $|g_{qk}|^2$ over a small range of $\omega_k \approx \omega_q$, that is, $\bar{g}_{qq}^2 \equiv \langle |g_{qk}|^2 \rangle_{\omega_k \approx \omega_q}$. Note that this approach is valid as long as the Markovian bath assumption holds. For a large but finite $N \sim \mathcal{O}(10^3)$, we also numerically check the time evolution of the cavity mode population, and extract the decay rates by fitting to an exponential profile. Our results show very good agreement with Eq. (2) [Appendix A].

It can be expected that increasing the wall thickness and/or tuning up the tweezer strength help isolation of the cavity from the rest of the ion crystal, and therefore the decay rate of a cavity mode decreases. This provides an extremely convenient way to setup the cavity because the state-of-the-art strongest tweezer strength is limited by about a few megahertz due to physical constraints of the atom energy configuration and laser power [23]. We further calculate the mode decay rates for an $N_S = 5$ cavity and presents the results in Fig. 1(b). A typical $\kappa \sim 10^{-3} \omega_0$ implies that the cavity mode can survive for about a thousand times of momentum exchanges before it vanishes.

Single-mode phonon lasing. – We now look into the phonon lasing mechanism of a resonator containing only $N_S = 1$ ion, which is pumped by lasers resonant with the blue side-band. Typically, the cavity mode frequency is about hundreds of kilohertz to a few megahertz, the sidebands are assumed resolvable from the carrier transition by Raman transitions of a few kilohertz in linewidth. We describe the evolution of the system by a master equation:

$$\dot{\rho} = -\frac{i}{\hbar} [H_S, \rho] - \sum_{\alpha=\pm} \frac{\kappa_{\text{th}}^\alpha}{2} \mathcal{L}_\alpha^\alpha[\rho] - \frac{\gamma}{2} \mathcal{L}_{\sigma^-}^-[\rho], \quad (3)$$

where ρ is the system density matrix governed by the system Hamiltonian $H_S/\hbar = -\delta_b \sigma_z/2 + \eta \Omega (a^\dagger \sigma^+ + \sigma^- a)$ in the rotating frame with $\sigma^- = |g\rangle\langle e|$ and $\sigma^+ = |e\rangle\langle g|$ the atomic lowering and raising operators, respectively, between the ground state $|g\rangle$ and excited $|e\rangle$ separated by energy $\hbar \omega_{eg}$; $\sigma_z = |e\rangle\langle e| - |g\rangle\langle g|$; γ is the natural linewidth; blue-side band detuning $\delta_b \equiv \omega_L - \omega_{eg} - \omega$ with driving laser frequency ω_L and cavity mode frequency ω ; η is the Lamb-Dicke parameter; Ω is the

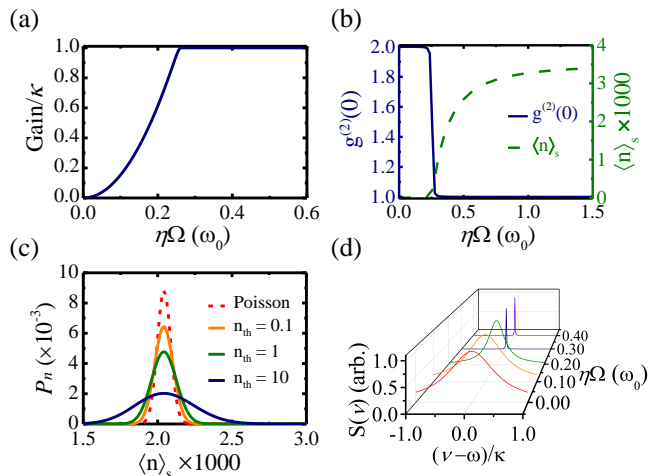


FIG. 2: (a) Gain as a function of driving strength in terms of $\eta\Omega$ on blue side-band resonance $\delta_b = 0$. The lasing threshold is at $\eta\Omega_c = 0.25\omega_0$. (b) Second-order coherence $g^{(2)}$ (left vertical axis) and the mean phonon number (right vertical axis) of the cavity mode for varied $\eta\Omega$. (c) Number distribution for $\eta\Omega = 0.4\omega_0 = 2\pi \times 0.2$ MHz with $\langle n \rangle_s = 2200$. The distribution is broadened by increasing the noise level. For comparison, the Poisson distribution ($n_{th} = 0$) is plotted in red dashed line. (d) Spectral lineshape for varied $\eta\Omega$ with the peak value normalized to one. In all cases (a)–(d), we choose $\kappa = 6.1 \times 10^{-3}\omega_0 = 2\pi \times 3.1$ kHz given by 2 + 2 tweezers of frequency $2\pi \times 2.4$ MHz. The cavity mode frequency $\omega = 2.0\omega_0 = 2\pi \times 1.0$ MHz. For (a), (b) and (d), all the results are under the noise level set by the Doppler temperature $n_{th} = 10$ corresponding to the $^{40}\text{Ca}^+$ ion with natural linewidth $\gamma = 2\pi \times 21.6$ MHz.

Raman Rabi frequency. The Lindblad superoperators are given by $\mathcal{L}_a^\pm[\rho] = a^\pm a^\mp \rho + \rho a^\pm a^\mp - 2a^\mp \rho a^\pm$ (here we denote $a^- = a$ and $a^+ = a^\dagger$ for convenience) and $\mathcal{L}_\sigma^-[\rho] = \sigma^+ \sigma^- \rho + \rho \sigma^+ \sigma^- - 2\sigma^- \rho \sigma^+$ with $\kappa_{th}^+ = n_{th}\kappa$ and $\kappa_{th}^- = (n_{th} + 1)\kappa$, where the noise level n_{th} accounts for nonzero cavity temperature contribution [24] and can be estimated by $n_{th} = [\exp(\hbar\omega/k_B T) - 1]^{-1}$. Note that the dynamics of the internal states are much faster than the motional ones, we can thus assume that the internal degrees of freedom adiabatically follow the motional operators. The dynamics of the phononic operator is of the form $\dot{a} = (\mathcal{G} - \kappa)a/2 + (\text{noise terms})$, which can be obtained by integrating the Heisenberg equations, with the gain given by

$$\mathcal{G} = \gamma \frac{s}{2} \langle \sigma_z \rangle = \sum_n \frac{\gamma s}{2(1 + ns)} P_n, \quad (4)$$

where $s = 2|\eta\Omega|^2 / [\delta_b^2 + (\gamma/2)^2]$. We take $\delta_b = 0$ for simplicity. To determine the population distribution, we recast the master equation (3) into the rate equations [Appendix B]:

$$\begin{aligned} \dot{P}_n = & - [\kappa_{th}^- n + \kappa_{th}^+ (n + 1)] P_n \\ & + \kappa_{th}^- (n + 1) P_{n+1} + \kappa_{th}^+ n P_{n-1} \\ & - \frac{\gamma s}{2} \left(\frac{n + 1}{1 + ns} P_n - \frac{n}{1 + (n - 1)s} P_{n-1} \right) \end{aligned} \quad (5)$$

for the probability P_n in the motional n state.

Figure 2 shows the gain as a function of pumping strength in the steady state, where we clearly see the lasing behavior with $\mathcal{G}/\kappa \rightarrow 1$ as the driving strength $\eta\Omega$ overpasses a threshold $\eta\Omega_c = 0.25\omega_0$. A typical timescale to lasing depends on the steady-state mean phonon number $\langle n \rangle_s$ built. For $\langle n \rangle_s \approx 2000$, it is about $14\kappa^{-1} \approx 2300\omega_0^{-1}$, comparable to 4.5 ms. To quantify the degree of lasing, we calculate $\langle n \rangle_s$ and second-order coherence $g^{(2)}(0) \equiv |\langle a^\dagger(0)a^\dagger(\tau)a(\tau)a(0) \rangle / \langle a^\dagger a \rangle^2}|_{\tau=0}$. The results are presented in Fig. 2(b). At low pumping level below the threshold, $g_{ph}^{(2)}(0)$ appears to be around 2 as the phonon number is small, suggesting a thermal chaotic phonon state. When $\eta\Omega > \eta\Omega_c$, the phonon number significantly builds up while the $g^{(2)}$ curve abruptly drops to unity, signaling the emergence of a coherent state, consistent with the gain profile.

The steady-state phonon number distribution is also obtained from Eq. (5) and plotted in Fig. 2(c), where we includes different profiles for various noise levels. At zero temperature, the distribution is exactly Poissonian. The rising noise level gradually broadens the distribution, becoming super-Poissonian. This is however commonly observed in ordinary optical lasers. We also investigate the line narrowing effect of the lasing mode. The lineshape is given by [Appendix C]

$$S(\nu) = \frac{\langle n \rangle_s}{(\nu - \omega)^2 + \Delta\nu^2/4}, \quad (6)$$

with $\Delta\nu = \kappa \frac{n_{th}}{\langle n \rangle_s} + \frac{\gamma}{2\langle n \rangle_s} \frac{s}{1 + \langle n \rangle_s s}$. One can see clearly from Fig. 2(d) that the spectral linewidth becomes narrowed when $\eta\Omega$ exceeds $\eta\Omega_c = 0.25\omega_0$ due to significant increase in the phonon number.

Two-mode phonon lasing. – We now consider a multi-mode cavity. Due to growing Hilbert space dimensions and limitation of computation power, we only focus on calculation for $N_S = 2$ in particular, which presents two longitudinal collective modes, the center-of-mass (COM) mode and the breath (BR) one. We apply on one of the two ions Raman laser beams to drive the blue-sideband resonances of the cavity modes. Typically, the frequency difference between the two modes is about hundreds of kilohertz so it can be assumed optically resolvable. However, two modes can exchange energy via the atomic excitation. This can be seen in the gain Eq. (4), where its linewidth is comparable to the atomic one ~ 20 MHz, making the result insensitive to the laser detuning. Also, due to the increasing number of coupled rate equations

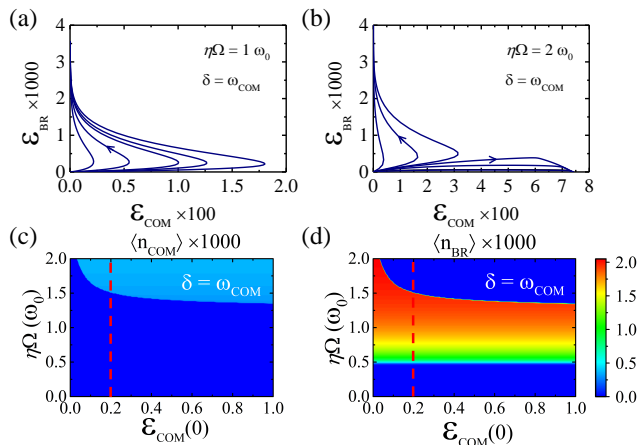


FIG. 3: Temporal trajectories showing the corresponding classical energy of the COM and BR modes of the two-mode resonator for (a) $\eta\Omega = 1.0\omega_0$, slightly above both thresholds $\eta\Omega_c^{\text{COM}} = 0.75\omega_0$ and $\eta\Omega_c^{\text{BR}} = 0.4\omega_0$, and (b) $\eta\Omega = 2.0\omega_0$, relatively stronger. In (a), every trajectory approaches to the BR mode with $\langle n_{\text{BR}} \rangle_s = 1780$. In (b), one group of trajectories approaches to $\langle n_{\text{BR}} \rangle_s = 2050$ and the other approaches to $\langle n_{\text{COM}} \rangle_s = 370$, depending on the choices of initial distribution of excitation (see text). (c) Phase diagram in terms of the COM phonon numbers and (d) the BR phonon numbers for keeping $\mathcal{E}_{\text{BR}}(0) = 0.5$, of both modes. For the non-lasing mode, the phonon number roughly corresponds to the thermal level $n_{\text{th,COM}} = 13$ and $n_{\text{th,BR}} = 8.2$. The line cuts correspond to the profiles discussed in Fig. 4.

becoming difficult to be managed, we turn to the Heisenberg equation method by considering the quadrature operators $X_q \equiv a_q^\dagger + a_q$ and $P_q \equiv i(a_q^\dagger - a_q)$ for $q = \text{COM}$ or BR . We leave the detailed derivation in Appendix D, and directly present the calculation results showing lasing of these modes given various parameters such as laser detuning, pump power, and starting energy characterized by initial $\langle X_j \rangle$ and $\langle P_j \rangle$.

The system dynamics can be characterized by a parameter corresponding to the classical energy associated with each mode:

$$\mathcal{E}_q(t) \equiv \frac{1}{2} [\langle X_q(t) \rangle^2 + \langle P_q(t) \rangle^2], \quad (7)$$

which is roughly 2 times of the mean phonon number by our convention. We now demonstrate an exemplary case with $w_L + w_R = 1 + 1$ tweezers of frequency $2\pi \times 3$ MHz, yielding $\omega_{\text{COM}} = 1.6\omega_0$ and $\omega_{\text{BR}} = 2.5\omega_0$ with decay rates $\kappa_{\text{COM}} = 0.05\omega_0$ and $\kappa_{\text{BR}} = 0.01\omega_0$, respectively; the thresholds from the single-mode calculation are given by $\eta\Omega_c^{\text{COM}} = 0.75\omega_0$ and $\eta\Omega_c^{\text{BR}} = 0.40\omega_0$. Note that here we have set $\eta_{\text{COM}} = \eta$ so that $\eta_{\text{BR}} = \sqrt{\omega_{\text{COM}}/\omega_{\text{BR}}}\eta$. We then depict the trajectories of \mathcal{E}_j for given lasing parameters starting from an initial state with specific energies $(\mathcal{E}_{\text{COM}}(0), \mathcal{E}_{\text{BR}}(0))$.

Here we only discuss the cases in particular where the driving strength surpasses the thresholds of both modes.

Our results show that the two modes cannot sustain lasing simultaneously. The emergence of lasing in one mode with significant excitation suppresses the other mode with vanishing phonon numbers. This can be seen in Fig. 3(a) and (b), where the trajectories terminate at one axis point. Explicitly, Fig. 3(a) shows a case where the driving strength is slightly above both thresholds. When the system starts from low excitations, both the modes grow in early stages, and evolve into a steady state in which only one mode survives while the other diminishes. Since $\eta\Omega_c^{\text{BR}} < \eta\Omega_c^{\text{COM}}$, it can be expected that the BR mode reaches lasing first and the COM mode is suppressed. Note that the final mean phonon number is determined from competition of the cavity loss and pumping so is independent from the choice of initial energies. When the pumping strength is sufficiently strong, at some point the trajectories develop into two groups corresponding to different lasing modes, as shown in Fig. 3(b). More energy distributed to one mode increases the likeliness of lasing of that mode.

It is helpful to look at the phases defined by the lasing modes in terms of phonon numbers as shown in Fig. 3(c) and (d). Here we map out the lasing phases by varying the driving strength and initial energy in the COM mode while keeping $\mathcal{E}_{\text{BR}}(0)$ constant. From weak to strong pumping strengths, we find that the system first undergoes a continuous lasing process favoring the BR mode, suppressing the COM mode, as discussed above. Interestingly, as pumping increases, up to some point the COM mode suddenly becomes dominant and prohibits the existence of the BR mode. Fig. 4(a) shows the population change following the line cuts in Fig. 3(c) and (d). The discontinuity of switching from the BR mode to the COM one signals a first-order phase transition [16]. We further calculate the second-order coherence for the two lasing regimes, and find that $g^{(2)}(0)$ closely follows the same trend as shown in Fig. 2(b) for the continuous lasing process. Across the sharp boundary, $g^{(2)}(0)$ also switches between 1 and 2 as the phonon number changes.

An interesting effect is that there is a $< 1\%$ residual excitation out of the phonon number of the non-lasing mode. Our calculation shows that this suppressed mode is forced to catch up with the frequency of the lasing one by looking at the classical coordinate $\langle X_q(t) \rangle$ for $q = \text{COM}$ or BR , as indicated in Fig 4(b). This phenomenon has been studied in the optomechanical two-membrane system [16], where this effect is visible because the lasing mode does not dominantly outnumber the non-lasing one, and the thermal noise level does not wash the signal out. In our system, however, we do not expect such synchronization to be detectable because of the significant thermal contribution.

Discussion and conclusion. – Finally, we examine the feasibility and conditions to observe the presented results in experiments. Take $^{40}\text{Ca}^+$ ions for example. For the single-mode lasing, we have reached the phonon number

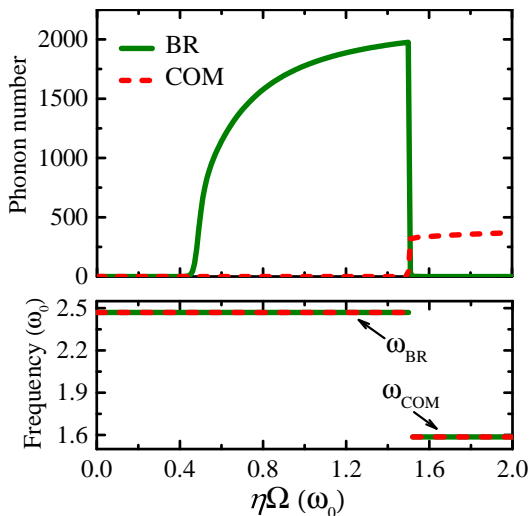


FIG. 4: (a) The phonon numbers of the COM and BR modes as the driving strength increases. The first continuous lasing process occurs at the usual threshold determined by the single-mode calculation. The sharp boundary emerges at $\eta\Omega = 1.5\omega_0$. (b) The frequencies of the two modes. Note that when $\eta\Omega < 1.5\omega_0$, the $\langle X_{\text{COM}}(t) \rangle$ (non-lasing mode) follows the frequency of the BR (lasing) mode. Their roles switch when $\eta\Omega > 1.5\omega_0$.

$\langle n \rangle_s \approx 2000$, which corresponds to a displacement of $0.7 \mu\text{m}$, in a timescale $2300\omega_0^{-1} \sim 4.5 \text{ ms}$. This suggests an ion crystal of comparable size ~ 2300 or longer before the reflected wave re-enters the system. We estimate for $\langle n \rangle_s \approx 500$ given by the condition with $1 + 1$ tweezers of frequency 3 MHz , the timescale reduces by an order as κ rises, the required size becomes < 300 . The corresponding displacement is $0.35 \mu\text{m}$, sufficiently larger than the thermal contribution $\sim 0.05 \mu\text{m}$.

To sum up, we have presented a tunable prototype of phonon laser based on an extremely simple architecture analogous to an ordinary optical resonator. The cavity walls are configurable on demand, controlled by arrangement of optical tweezers with flexible parameters. As long as the Markovianity holds, which can be secured by strong enough tweezers, the lasing mechanism is governed by a master equation, which we have utilized to calculate the properties including the $g^{(2)}$ coherence, number distribution, and spectral lineshape. All the results are presented based on finite temperature calculation set by the Doppler cooling, suggesting the feasibility in experiments. For the two-mode case, we have developed the dynamical equations for quadrature operators of the normal modes. We also demonstrated the lasing mode competition, and mapped out the phase diagram for the surviving mode. We expect that the proposed scheme and mathematical methods used apply to more ion cases, which may yield richer unexplored effects.

APPENDIX

Appendix A: Decay rates of cavity modes

In this section we present the detailed calculation of the effective decay rates for the cavity phonon modes. We divide the system into the cavity part (C) and the environment (B) so that the motional Hamiltonian under the harmonic approximation reads

$$\begin{aligned}
 H_m = & \underbrace{\sum_{i \in C} \frac{p_i^2}{2m} + \sum_{i,j \in C} A_{ij} z_i z_j}_{H_m^C} \\
 & + \underbrace{\sum_{i \in B} \frac{p_i^2}{2m} + \sum_{i,j \in B} A_{ij} z_i z_j}_{H_m^B} + \underbrace{\sum_{i \in C, j \in B} A_{ij} z_i z_j}_{V_m^{CB}}, \quad (\text{A1})
 \end{aligned}$$

where the elements A_{ij} form the coupling matrix $\mathbf{A} = \mathbf{A}_C \oplus \mathbf{A}_B + \mathbf{A}_{CB}$, where \mathbf{A}_C and \mathbf{A}_B are $N_C \times N_C$ and $(N - N_C) \times (N - N_C)$ submatrices describing the coupling within the cavity part and environment, respectively; \oplus denotes the direct sum and \mathbf{A}_{CB} is an $N_C \times (N - N_C)$ matrix containing the interaction between the two subsystems. Each subsystem's coupling matrix can be diagonalized separately to find the normal modes represented by the annihilation and creation operator pair: (a_q, a_q^\dagger) for the cavity part, where the mode index $q = 1, \dots, N_C$ with $N_C = N_S + w_R + w_L$ the number of ions participating in the cavity and two walls; (a_k, a_k^\dagger) for the environment, where the mode index $k = 1, \dots, N - N_C$ with N the total number of ions of the entire array. Note that here we also include the tweezered ions in the subsystem C in order to retain the smoothness of the dispersion relation of the bath and secure the Markovianity. However, by doing so, the subsystem C has $w_L + w_R$ more modes than the supposed N_S ones. Fortunately, those $w_L + w_R$ modes mainly resulting from tweezered ions are well separated from the others in frequency, corresponding to spatial wavevectors very localized on the tweezered sites. This allows us to identify the rest as the cavity modes with one-to-one correspondence. In the discussion of phonon lasing, we will only focus on these cavity modes.

Under the rotating wave approximation, the Hamiltonian (A1) can then be re-written into

$$\begin{aligned}
 H_m = & \sum_{q=1}^{N_C} \hbar\omega_q a_q^\dagger a_q + \sum_{k=1}^{N-N_C} \hbar\omega_k a_k^\dagger a_k \\
 & + \sum_{q \in C, k \in B} g_{qk} (a_q a_k^\dagger + a_k a_q^\dagger), \quad (\text{A2})
 \end{aligned}$$

where ω_q and ω_k are the eigenfrequencies of the cavity and environment modes, respectively, and g_{qk} deals with the coupling matrix between mode q in C and mode k

in B . Explicitly, $g_{qk} = \frac{\hbar}{2m} \sum_{ij} U_{C,qi}^T A_{ij} U_{B,jk} / \sqrt{m^2 \omega_q \omega_k}$ also forms an $N_C \times (N - N_C)$ matrix, where U_C and U_B are the transformation matrices that diagonalize \mathbf{A}_C and \mathbf{A}_B , respectively.

The Heisenberg equations of motion for the field operators then read

$$\dot{a}_q = -i\omega_q a_q - i \sum_{k \in B} g_{qk} a_k \quad (\text{A3})$$

$$\dot{a}_k = -i\omega_k a_k - i \sum_{q \in C} g_{qk} a_q. \quad (\text{A4})$$

By integrating out the bath's degrees of freedom, we obtain the following equation for mode $q \in C$:

$$\begin{aligned} \dot{a}_q &= -i\omega_q a_q - i \sum_{k \in B} g_{qk} a_k(0) e^{-i\omega_k t} \\ &\quad - \sum_{k \in B} |g_{qk}|^2 a_q \int_0^t dt' e^{-i(\omega_k - \omega_q)(t-t')}. \end{aligned} \quad (\text{A5})$$

The first term contributes to noise and the second term corresponds to the decay process, which can be characterized by the rate:

$$\kappa_q \approx 2 \sum_{k \in B} |g_{qk}|^2 \int_0^\infty dt' e^{-i(\omega_k - \omega_q)t'} \approx 2\pi \bar{g}_{qq}^2 \rho_B(\omega_q). \quad (\text{A6})$$

For a given finite N , since the cavity and environment degrees of freedom are both discrete and these modes may not overlap, we have calculated the above summation numerically by plugging in the actual parameters. As long as $N \gg N_C$, we find the results have been found to be consistent with the last approximation, where we have taken the continuum limit and numerically computed the density of states $\rho_B(\omega)$ for the bath's degrees, and obtained \bar{g}_{qq}^2 by coarse-graining $|g_{qk}|^2$ over a small range of $\omega_k \approx \omega_q$, that is, $\bar{g}_{qq}^2 \equiv \langle |g_{qk}|^2 \rangle_{\omega_k \approx \omega_q}$. This amounts to justification of validity of Markov approximation. Also, it should be emphasized that here we only focus on longitudinal modes so that the bath modes constitute a broadband-like spectrum. The approximation breaks down for transverse modes for its extreme narrow-band spectral structure.

To verify our calculation, we also look at the real-time population profile numerically by explicitly including the all motional degrees of the entire array without approximation. As shown in Fig. 5, when the tweezer frequency is not strong enough compared to ω_0 , we find visible large oscillations causing a certain degree of non-Markovianity. But the non-Markovianity can be gradually removed when we increase the tweezer frequency up to approximately an order of magnitude larger than ω_0 . In Fig. 5(d), where $\omega^{ot}/\omega_0 = 5.9$, we recover the evolution based on Markovian bath assumption.

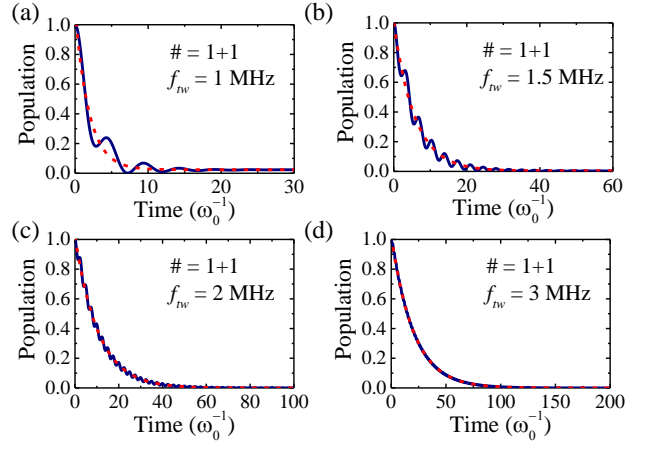


FIG. 5: We show the real-time population profiles (blue curves) of a single-ion resonator given varied tweezer frequencies. These curves are fitted to exponential profiles (red dashed lines) characterized by the decay rates calculated according to Eq. (A6). These results are based on calculation considering an ion crystal of more than 1000 $^{40}\text{Ca}^+$ ions with ion separation $7 \mu\text{m}$.

Appendix B: Probability rate equation and gain

In this section, we derive the master equation and the corresponding probability rate equations considering the phonon cavity being pumped by blue-sideband lasers. To simplify our discussion, here we only focus on the single mode case with $N_S = 1$ ion. Under the Lamb-Dicke approximation, the Heisenberg equations of motion for the relevant operators are given by

$$\dot{a} = -\frac{\kappa}{2} a - i\eta\Omega\sigma^+ \quad (\text{B1})$$

$$\dot{\sigma}^+ = \left(-i\delta_b - \frac{\gamma}{2}\right) \sigma^+ - i\eta\Omega a\sigma_z \quad (\text{B2})$$

$$\dot{\sigma}_z = -\gamma(\sigma_z + 1) + 2i\eta\Omega(\sigma^- a - a^\dagger \sigma^+) \quad (\text{B3})$$

where $\sigma^- = |g\rangle\langle e|$ and $\sigma^+ = |e\rangle\langle g|$ are the atomic lowering and raising operators, respectively, between the ground state $|g\rangle$ and excited $|e\rangle$ separated by energy $\hbar\omega_{eg}$; $\sigma_z = |e\rangle\langle e| - |g\rangle\langle g|$; γ is the natural linewidth; blue side-band detuning $\delta_b \equiv \omega_L - \omega_{eg} - \omega$ with driving laser frequency ω_L and cavity mode frequency ω ; η is the Lamb-Dicke parameter; Ω is the Raman Rabi frequency. Note that the dynamics of the internal states are much faster than the motional ones, we can thus assume that the internal degrees of freedom adiabatically follow the motional operators. By taking $\dot{\sigma}^+ \approx 0$, we immediately obtain

$$\sigma^+ \approx -\frac{\eta\Omega a\sigma_z}{\delta_b - i\frac{\gamma}{2}} \quad (\text{B4})$$

and therefore

$$\dot{a} = -\frac{\kappa}{2}a - \frac{1}{2} \frac{\gamma |\eta\Omega|^2}{\delta_b^2 + (\frac{\gamma}{2})^2} \sigma_z a + \text{shift} + \text{noise}. \quad (\text{B5})$$

Note that the noise term must be present in order to assure a a valid field operator that satisfies $[a, a^\dagger] = 1$. Both the shift and noise terms are irrelevant for current discussion. The gain can now be identified as

$$\mathcal{G} = -\frac{\gamma |\eta\Omega|^2}{\delta_b^2 + (\frac{\gamma}{2})^2} \sigma_z. \quad (\text{B6})$$

Also, by substitution of Eq. (B4) into Eq. (B3) as $\dot{\sigma}_z \approx 0$, we have

$$\begin{aligned} \sigma_z &= -\left(I + \frac{2}{\delta_b^2 + (\frac{\gamma}{2})^2} |\eta\Omega|^2 a^\dagger a \right)^{-1} \\ &= -\sum_n \frac{1}{1+ns} |n\rangle \langle n| \end{aligned} \quad (\text{B7})$$

and

$$\eta\Omega\sigma^+ = \frac{s}{2}(\delta_b + i\gamma)b \quad (\text{B8})$$

where $s = \frac{2|\eta\Omega|^2}{\delta_b^2 + (\frac{\gamma}{2})^2}$ and $b \equiv \sum_n \frac{\sqrt{n+1}}{1+ns} |n\rangle \langle n+1|$. Plugging the atomic operators back to the master equation Eq. (3) in the main text, we finally arrive at

$$\begin{aligned} \dot{P}_n &= -\frac{\kappa}{2} (n_{\text{th}} + 1) (2nP_n - 2(n+1)P_{n+1}) \\ &\quad - \frac{\kappa}{2} n_{\text{th}} (2(n+1)P_n - 2nP_{n-1}) \\ &\quad - \frac{\gamma s}{2} \left(\frac{n+1}{1+ns} P_n - \frac{n}{1+(n-1)s} P_{n-1} \right). \end{aligned} \quad (\text{B9})$$

Here, we have added the thermal contribution characterized by the noise level n_{th} , which can be estimated by $n_{\text{th}} = [\exp(\hbar\omega/k_B T) - 1]^{-1}$ [24]. In the steady-state, the probability can be computed

$$P_n = P_0 \prod_{k=1}^n \frac{\kappa n_{\text{th}} + \frac{1}{2} \frac{\gamma s}{1+(k-1)s}}{\kappa (n_{\text{th}} + 1)} \quad (\text{B10})$$

with P_0 the normalization factor such that $\sum_n P_n = 1$.

Appendix C: Line narrowing

To find out the spectral lineshape of the phonon field, we first look at the mean phonon number equation $d\langle a^\dagger a \rangle / dt = \sum_n n \dot{P}_n$. By substitution of Eq. (B9), we

obtain [24]

$$\begin{aligned} \frac{d}{dt} \langle n \rangle &= \sum_n \left\{ \left(\frac{\gamma}{2} \frac{s}{1+n \cdot s} - \kappa \right) n P_n \right. \\ &\quad \left. + \left(\kappa n_{\text{th}} + \frac{\gamma}{2} \frac{s}{1+ns} \right) P_n \right\} \\ &\approx \left(\frac{\gamma}{2} \frac{s}{1+\langle n \rangle s} - \kappa \right) \langle n \rangle \\ &\quad + \kappa n_{\text{th}} + \frac{\gamma}{2} \frac{s}{1+\langle n \rangle s}, \end{aligned} \quad (\text{C1})$$

where we have approximated n in the denominator of the summand by its instantaneous mean value $\langle n \rangle$. We thus can identify the gain $\mathcal{G}(t) = \frac{\gamma}{2} \frac{s}{1+\langle n \rangle s}$, consistent with Eq. (B6) except n is taken to be the mean value. In the steady state, $\langle n \rangle \rightarrow \langle n \rangle_s$, and

$$\mathcal{G} \rightarrow \kappa \left(1 - \frac{n_{\text{th}}}{\langle n \rangle_s} \right) - \frac{\gamma}{2 \langle n \rangle_s} \frac{s}{1+\langle n \rangle_s s}. \quad (\text{C2})$$

On the other hand, the Langevin equation reads

$$\dot{a}(t) = \left[\mathcal{G} - \left(\frac{\kappa}{2} + i(\omega - \nu) \right) \right] a(t) + \text{noise terms}, \quad (\text{C3})$$

where ν is the probe frequency understood as a Fourier component. By the quantum regression theorem, we can acquire the spectral lineshape

$$\begin{aligned} S(\nu) &= \mathcal{F}[\langle a^\dagger(\tau) a(0) \rangle] \\ &= \frac{\langle n \rangle_s}{(\nu - \omega)^2 + \Delta\nu^2/4}, \end{aligned} \quad (\text{C4})$$

with $\Delta\nu = \kappa \frac{n_{\text{th}}}{\langle n \rangle_s} + \frac{\gamma}{2 \langle n \rangle_s} \frac{s}{1+\langle n \rangle_s s}$, and \mathcal{F} denotes the Fourier transform.

Appendix D: Model for phonon lasing - two mode

The rate equation approach summarized in Sec. B also applies to multi-mode cavities. However, the dimension of the required Hilbert space grows exponentially with the number of modes, making the calculation intractable even for $N_S = 2$. Here, we adopt another method based on the normal-mode quadrature operators [16].

The Hamiltonian that describes the two-mode phonon cavity reads

$$H/\hbar = -\frac{\delta}{2} \sigma_i^z + \sum_q \omega_q a_q^\dagger a_q + \sum_{i,q} \frac{\eta_q \Omega_i}{\sqrt{2}} (\sigma_i^+ a_q^\dagger + a_q \sigma_i^-) \quad (\text{D1})$$

where $\delta = \omega_L - \omega_{eg}$; a_q and a_q^\dagger are phonon field operators of the q th cavity mode; σ_i^- and σ_i^+ are atomic operators of the i th atom driven by a laser of frequency ω_L and Rabi frequency Ω_i ; η_q is the corresponding Lamb-Dicke parameter of the q th mode. Now, the normal-mode quadrature operators are defined

Then the Langevin equations of the quadrature operators of different orders are given by

$$\begin{cases} X_q = a_q^\dagger + a_q \\ P_q = i(a_q^\dagger - a_q). \end{cases} \quad (\text{D2})$$

$$\begin{aligned} \frac{d}{dt} (P_q^n X_q^m) = & -n\omega_q (P_q^{n-1} X_q^{m+1} + i(n-1) P_q^{n-2} X_q^m) \\ & + m\omega_q (P_q^{n+1} X_q^{m-1} + i(m-1) P_q^n X_q^{m-2}) \\ & - \frac{1}{2}\kappa_q n P_q^n X_q^m + \frac{1}{2}\kappa_q (2n_{\text{th},q} + 1) (n(n-1) P_q^{n-2} X_q^m) \\ & - \frac{1}{2}\kappa_q m P_q^n X_q^m + \frac{1}{2}\kappa_q (2m_{\text{th},q} + 1) (m(m-1) P_q^n X_q^{m-2}) \\ & - n \sum_{i,q} \frac{\eta_q \Omega_i}{\sqrt{2}} (\sigma_i^- + \sigma_i^+) P_q^{n-1} X_q^m \\ & - im \sum_{i,q} \frac{\eta_q \Omega_i}{\sqrt{2}} (\sigma_i^- - \sigma_i^+) P_q^n X_q^{m-1}, \end{aligned} \quad (\text{D3})$$

$$\frac{d}{dt} \sigma_i^- = \left(i\delta - \frac{\gamma}{2}\right) \sigma_i^- + i \frac{1}{2} \sum_q \frac{\eta_q \Omega_i}{\sqrt{2}} \sigma_{z,i} (X_q - iP_q), \quad (\text{D4})$$

$$\frac{d}{dt} \sigma_{z,i} = -\gamma(\sigma_{z,i} + 1) - i \sum_q \frac{\eta_q \Omega_i}{\sqrt{2}} (\sigma_{z,i}^+ (X_q - iP_q) - \text{H.c.}) \quad (\text{D5})$$

Note that different modes decay independently but are still coupled through sharing the atomic states, as revealed by the last terms of Eqs. (D4) and (D5). The second-order coherence can be calculated directly by $g_q^{(2)}(0) = (\langle n_q^2 \rangle - \langle n_q \rangle^2) / \langle n_q \rangle^2$, where

$$\langle n_q \rangle = \frac{1}{4} (\langle X_q^2 \rangle + \langle P_q^2 \rangle) - \frac{1}{2} \quad (\text{D6})$$

and

$$\begin{aligned} \langle n_q^2 \rangle = & \frac{1}{16} (\langle X_q^4 \rangle + \langle P_q^4 \rangle + 2\text{Re} \langle P_q^2 X_q^2 \rangle) \\ & - \frac{1}{4} (\langle X_q^2 \rangle + \langle P_q^2 \rangle + 2\text{Im} \langle P_q X_q \rangle + 1). \end{aligned} \quad (\text{D7})$$

Acknowledgments

We thank the support from MOST of Taiwan under Grant No. 109-2112-M-002-022 and National Taiwan University under Grant No. NTU-CC-109L892006. GDL thanks Ming-Shien Chang and Mishkat Bhattacharya for valuable discussion and feedback.

- [2] K. Vahala, M. Herrmann, S. Knünz, V. Batteiger, G. Saathoff, T. W. Hänsch, and T. Udem, *Nature Physics* **5**, 682 (2009).
- [3] S. Knünz, M. Herrmann, V. Batteiger, G. Saathoff, T. W. Hänsch, K. Vahala, and T. Udem, *Phys. Rev. Lett.* **105**, 013004 (2010).
- [4] M. Ip, A. Ransford, A. M. Jayich, X. Long, C. Roman, and W. C. Campbell, *Phys. Rev. Lett.* **121**, 043201 (2018).
- [5] J. Kabuss, A. Carmele, T. Brandes, and A. Knorr, *Phys. Rev. Lett.* **109**, 054301 (2012).
- [6] J. Kabuss, A. Carmele, and A. Knorr, *Phys. Rev. B* **88**, 064305 (2013).
- [7] A. Khaetskii, V. N. Golovach, X. Hu, and I. Žutić, *Phys. Rev. Lett.* **111**, 186601 (2013).
- [8] I. S. Grudin, H. Lee, O. Painter, and K. J. Vahala, *Phys. Rev. Lett.* **104**, 083901 (2010).
- [9] R. P. Beardsley, A. V. Akimov, M. Henini, and A. J. Kent, *Phys. Rev. Lett.* **104**, 085501 (2010).
- [10] I. Mahboob, K. Nishiguchi, A. Fujiwara, and H. Yamaguchi, *Phys. Rev. Lett.* **110**, 127202 (2013).
- [11] U. Kemiktarak, M. Durand, M. Metcalfe, and J. Lawall, *Phys. Rev. Lett.* **113**, 030802 (2014).
- [12] H. Jing, S. K. Özdemir, X.-Y. Lü, J. Zhang, L. Yang, and F. Nori, *Phys. Rev. Lett.* **113**, 053604 (2014).
- [13] J. Zhang, B. Peng, Ş. K. Özdemir, K. Pichler, D. O. Krimer, G. Zhao, F. Nori, Y.-x. Liu, S. Rotter, and L. Yang, *Nature Photonics* **12**, 479 (2018).
- [14] Y. Jiang, S. Maayani, T. Carmon, F. Nori, and H. Jing, *Phys. Rev. Applied* **10**, 064037 (2018).
- [15] R. M. Pettit, W. Ge, P. Kumar, D. R. Luntz-Martin, J. T. Schultz, L. P. Neukirch, M. Bhattacharya, and A. N.

[1] J. I. Cirac and P. Zoller, *Phys. Rev. Lett.* **74**, 4091 (1995).

- Vamivakas, *Nature Photonics* **13**, 402 (2019).
- [16] J. Sheng, X. Wei, C. Yang, and H. Wu, *Phys. Rev. Lett.* **124**, 053604 (2020).
- [17] J. B. Khurgin, M. W. Pruessner, T. H. Stievater, and W. S. Rabinovich, *Phys. Rev. Lett.* **108**, 223904 (2012).
- [18] Y.-C. Shen and G.-D. Lin, *New Journal of Physics* **22**, 053032 (2020).
- [19] J. I. Cirac and P. Zoller, *Nature* **404**, 579 (2000).
- [20] A. K. Ratcliffe, R. L. Taylor, J. J. Hope, and A. R. Carvalho, *Physical Review Letters* **120**, 1 (2018), [arXiv:1711.05875](https://arxiv.org/abs/1711.05875) .
- [21] S. Jain, J. Alonso, M. Grau, and J. Home, *Physical Review X* **10**, 10.1103/physrevx.10.031027 (2020).
- [22] S.-L. Zhu, C. Monroe, and L.-M. Duan, *Phys. Rev. Lett.* **97**, 050505 (2006).
- [23] S. Saskin, J. Wilson, B. Grinkemeyer, and J. Thompson, *Physical Review Letters* **122**, 10.1103/physrevlett.122.143002 (2019).
- [24] M. S. Pierre Meystre, *Elements of Quantum Optics* (Springer-Verlag Berlin Heidelberg, 2007).